Journal of Magnetic Resonance 315 (2020) 106738

Contents lists available at ScienceDirect

Journal of Magnetic Resonance

journal homepage: www.elsevier.com/locate/jmr

Homogeneous fields: Double expansion method, 3D printing/CNC realization, and verification by atomic magnetometry

Daniel A. Rodriguez Castillo, Jaafar N. Ansari, Robert J. Cooper, Garrett J. Lee, David W. Prescott, Karen L. Sauer *

Department of Physics and Astronomy, Quantum Science and Engineering Center, George Mason University, Fairfax, VA 22030, United States

ARTICLE INFO

Article history:
Received 13 March 2020
Revised 23 April 2020
Accepted 24 April 2020
Available online 1 May 2020

Keywords:
NQR
Low-field
Homogeneous
Field design
3D printing
Atomic magnetometers

ABSTRACT

In low-field magnetic resonance applications there is often an interest in creating homogeneous magnetic fields over unusual geometries, particularly when quantum magnetometers are involved. In this paper a design method is proposed, where both the surface current and magnetic field are expanded to find current coefficients that cancel out higher order field terms. Two coils are designed using this double expansion methodology: (1) a tuning field for a half-meter-long atomic magnetometer array and (2) a null field for a magnetometer to operate adjacent to an excitation solenoid. The field verification of the former shows the accuracy of CNC milling and the method proposed; a close analysis of the field signature in the latter revealed the limitations of 3D printing for precise scientific applications. Both coils are designed to be fifth-order error systems or better.

1. Introduction

In conventional NMR, where high fields are created with superconducting magnets, excitation and field correction coils are wrapped around cylinders to fit in the magnet bore. In low-field magnetic resonance, however, it can be advantageous to deviate from the cylindrical shape, depending on the application [1–10]. Furthermore, field coils are used to create not only the excitation, but also the static tuning field. Both field strength and homogeneity are required for sensitive measurements. The focus of the method described here is the design of homogeneous fields for applications where unconventional geometries are required.

Many methods have been applied to design homogeneous fields. The methodologies have often been driven in large measure by the need for efficient gradient coils in magnetic resonance imaging [11–14]. A common strategy is to expand the field in a series about the point of interest and cancel out as many higher order terms as feasible. In the case of axially symmetric systems where the target point is at the center, the expansion in terms of zonal harmonics, $r^l P_l(\cos\theta)$, is particularly elegant [15]. For systems lacking this symmetry, the Taylor series expansion can serve more generally. Many systems built on the field-expansion methodology use the geometry of a fixed number of coils to eliminate the higher order terms. For example, the Helmholtz pair cancels the second order derivative of the field along the axis by fixing the separation of the coils to be equal to the radius of the coil [16]. The first and third order derivatives are zero from symmetry, thus the Helmholtz coil is a fourth-order error system in the axial field. Higher order terms can be canceled, but at the expense of more coils [17–21]. More recently, particle swarm optimization has successfully been used to create homogeneous fields with a fixed numbers of coils and under geometric constraints [22]. The simplicity of the Helmholtz pair, and similar implementations with a small number of coils, makes such designs appealing, but the geometrical requirements can be overly restrictive for some applications.

An alternate method, known as the target-field method [23–25] gives a relatively straight-forward connection between the desired field and the surface current distribution by relating the Fourier transform of the field to that of the surface current. Exact solutions can be found for an infinitely long cylinder [26,27] or infinitely large planes [24,28]. Truncation of the geometry [29,30], however, can come at the cost of the desired field. In addition, designed surface currents may be quite complex, including both axial and azimuthal components for the cylinder, as well as radial and azimuthal components for the planar coil. Here we focus on homogeneous fields produced by a solenoid with an arbitrary cross-section and length. We further restrict ourselves to

* Corresponding author.
E-mail address: ksauer1@gmu.edu (K.L. Sauer).

https://doi.org/10.1016/j.jmr.2020.106738
1090-7807/

non-axial surface currents, which can simplify the construction. Therefore, this methodology is useful for the creation of homogeneous fields with relatively easy-to-construct coils with a fixed geometry.

Perturbation from a uniform circular solenoid was first implemented with the addition of outer or inner notches [31–33] to improve homogeneity at the center. Multiple layers of windings are used in these designs, which can lead to strong capacitive coupling between windings and unwanted self-resonant behavior at low frequencies [34]. The surface current in the work described here is created by changing the density of the windings, not through multiple layers of wires.

Other methods also allow for a variable surface current, but employ computationally intensive techniques. For example, the matrix inversion methods minimize the field deviation at a discrete number of points with a discrete number of wires or surface elements [35–38]. In the work described here, the surface current is expressed as a series expansion around a uniform surface current. The order of the expansion is matched to the number of higher order terms in the field's Taylor series that are to be canceled out. Equivalent cancellations conditions, such as those related by symmetry, are excluded. Further detail on the nature of these equivalent conditions is given in the theory section. The computations are not intensive since relatively few terms, and therefore variables, are needed.

The proposed methodology is applied to two systems: (1) a wide rectangular coil for tuning a linear array of magnetometers used to map magnetic fields [8] and (2) a solenoid with a leakage field small enough to allow for measurements with an external magnetometer [39]. Sketches of the systems are shown in Fig. 1. Both examples are focused on detecting radio-frequency RF signals, as from nuclear quadrupole resonance NQR [40], with a goal of getting the magnetometers as close as possible to the sample of interest. The rectangular coil design is based on two infinite current ribbons which gives a sixth-order error system in B_z, where z is the central axis of the tuning field. The solenoid is designed to be a fifth-order error system for the external radial field at its midpoint. The radial field here is zero by symmetry. Then if the magnetometer is oriented to be insensitive to the axial field, it is homogeneously shielded from excitation.

Construction is based around discrete wires placed in guided slots, as opposed to flexible printed circuits with limited copper thickness, to avoid limitations at high power. In the first application a computer driven milling machine is used to create these slots, and in the second 3D stereolithography printing is used. The relationship between the construction techniques and the designed homogeneity is discussed.

2. Theory

We start with a continuously varying surface current density $\mathbf{K}$ and then later discretize this to turns of wire. The surface current is taken to be perpendicular to the z-axis, neglecting the small component along z when using a single piece of wire to wind the coil, as is usual. It is further proscribed to run over a tube of length L with arbitrary cross section and can be expressed as $\mathbf{K} = K(z)\hat{t}$, where $\hat{t}$ is tangential to the surface. A magnetic field component along $\hat{x}_i$ at a position $\mathbf{r}$ can then be expressed, using the Biot-Savart's Law, as

$$B_i(\mathbf{r}) = \int_{-L/2}^{L/2} K(z')\Phi(\mathbf{r},z')dz', \tag{1}$$

with

$$\Phi(\mathbf{r},z') \equiv \frac{\mu_0}{4\pi}\oint \frac{[\hat{t}\times(\mathbf{r}-\mathbf{r}')]\cdot\hat{x}_i}{|\mathbf{r}-\mathbf{r}'|^3}dt', \tag{2}$$

integrated over the perimeter of the tube cross-section. Notice that the function $\Phi(\mathbf{r},z')$ contains all the geometric information, and has been separated out from the surface current which is to be designed so as to maximize field homogeneity.

In order to facilitate the design of the surface current, K, it can be expanded in a set of basis functions $f_n(z)$:

$$K(z) = K_0\left(1+\sum_{n=1}^{N}\lambda_n f_n(z)\right). \tag{3}$$

For example, $f_n(z)$ could be $\cos\{(2n-1)\pi\frac{z}{L}\}$ or $(z/L)^{2n}$ for a symmetric system. Then, using Eqs. (1) and (3):

$$B_i(\mathbf{r}) = K_0\left(\int_{-L/2}^{L/2}\Phi(\mathbf{r},z')dz' + \sum_{n=1}^{N}\lambda_n\int_{-L/2}^{L/2}f_n(z')\Phi(\mathbf{r},z')dz'\right). \tag{4}$$

The components of the magnetic field B_i can be expanded in a Taylor series expansion around the position of interest $\mathbf{r_0}$

$$\begin{aligned} B_i(\mathbf{r_0}+\mathbf{a}) &= B_i(\mathbf{r}_0) + \sum_{j=1}^{\infty}\left[\frac{1}{j!}(\mathbf{a}\cdot\nabla_{\mathbf{r}})^j B_i(\mathbf{r})\right]_{\mathbf{r}=\mathbf{r_0}} \\ &= B_i(\mathbf{r}_0) + K_0\sum_{j=1}^{\infty}\frac{1}{j!}\left\{\int_{-L/2}^{L/2}\left[(\mathbf{a}\cdot\nabla_{\mathbf{r}})^j\Phi(\mathbf{r},z')\right]_{\mathbf{r}=\mathbf{r_0}}dz'\right. \\ &\quad \left. + \sum_{n=1}^{N}\lambda_n\int_{-L/2}^{L/2}f_n(z')\left[(\mathbf{a}\cdot\nabla_{\mathbf{r}})^j\Phi(\mathbf{r},z')\right]_{\mathbf{r}=\mathbf{r_0}}dz'\right\}, \end{aligned} \tag{5}$$

where in the second line we have used Eq. (4). The terms in the summation represent the perturbation of the field from uniform as a function of the displacement $\mathbf{a} = a_1\hat{x} + a_2\hat{y} + a_3\hat{z}$ from $\mathbf{r}_0$. Getting a homogeneous field to the jth order requires that, for all values of j and below, the two terms in curly brackets must be equal and opposite, giving constraints on $K(z)$ through λ_n . For instance, for a first order solution, $j = 1$, there could be a maximum of three constraints on $K(z)$ corresponding to $[a_1, a_2, a_3]$. The number of coefficients λ and terms in the expansion of surface current, N, is chosen to equal the number of distinct constraints. Excluded are repeat conditions and the trivial solution where both terms in brackets are zero. For example, to get a homogeneous field to $j = 2$, a constraint occurs with every pairing of the two components $a_p a_q$:

$$\begin{aligned} a_p a_q\left(\int_{-L/2}^{L/2}\left[\frac{\partial^2\Phi(\mathbf{r},z')}{\partial x_p\partial x_q}\right]_{\mathbf{r}=\mathbf{r_0}}dz' + \sum_{n=1}^{N}\lambda_n\int_{-L/2}^{L/2}f_n(z')\left[\frac{\partial^2\Phi(\mathbf{r},z')}{\partial x_p\partial x_q}\right]_{\mathbf{r}=\mathbf{r_0}}dz'\right) \\ = 0, \end{aligned} \tag{6}$$

where $x_1 = x, x_2 = y$, and $x_3 = z$.

The number of constraints, again excluding repeat conditions and trivial solutions, then grow, setting a new required value of N in Eq. (3). If this is the final constraint to be applied, this can be rewritten as

$$b_N - \sum_{n=1}^{N}\lambda_n c_{Nn} = 0 \quad \text{where} \tag{7}$$

$$b_N \equiv \int_{-L/2}^{L/2}\left[\frac{\partial^2\Phi(\mathbf{r},z')}{\partial x_p\partial x_q}\right]_{\mathbf{r}=\mathbf{r_0}}dz' \quad \text{and} \tag{8}$$

$$c_{Nn} \equiv -\int_{-L/2}^{L/2}f_n(z')\left[\frac{\partial^2\Phi(\mathbf{r},z')}{\partial x_p\partial x_q}\right]_{\mathbf{r}=\mathbf{r_0}}dz'. \tag{9}$$

In this way a system of equations can be built up:

$$C\boldsymbol{\lambda} = \mathbf{b} \tag{10}$$

where

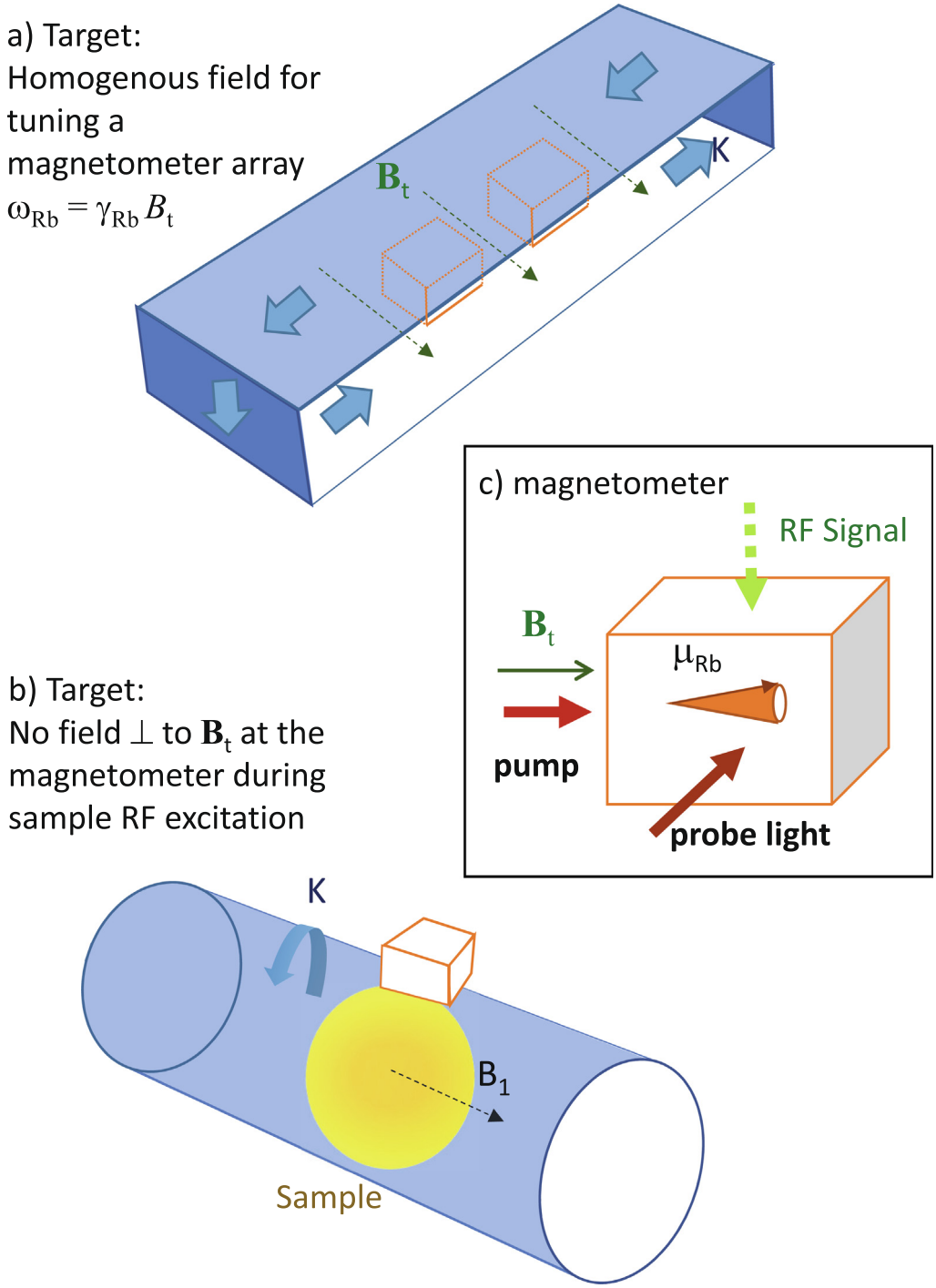

Fig. 1. Example systems benefiting from field coil design: a) a homogeneous tuning field B_t is required for narrow linewidth, and therefore sensitivity, of a magnetometer array b) an excitation coil with a small leakage field avoids saturation of an external magnetometer placed to measure the NMR/NQR signal from a sample. Inset (c) shows the basic magnetometer operation: optically pumped ^{87}Rb is probed when an RF signal sets the magnetic moment μ_{Rb} precessing. As in NMR, the precession occurs only for RF signals close to the Larmor frequency ω_{Rb} and transverse to $\mathbf{B}_t$.

$$C \equiv \begin{bmatrix} c_{11} & c_{12} & \cdots & c_{1N} \\ c_{21} & c_{22} & \cdots & c_{2N} \\ \vdots & \vdots & \vdots & \vdots \\ c_{N1} & c_{N2} & \cdots & c_{NN} \end{bmatrix}, \boldsymbol{\lambda} \equiv \begin{bmatrix} \lambda_1 \\ \lambda_2 \\ \vdots \\ \lambda_N \end{bmatrix}, \mathbf{b} \equiv \begin{bmatrix} b_1 \\ b_2 \\ \vdots \\ b_N \end{bmatrix},$$

where the first subscript corresponds to the m^{th} constraint out of N and the second subscript corresponds to the n^{th} basis function. Identical constraints coming from different derivatives are not included so that the matrix C is square and full rank and therefore invertible so the solution $\boldsymbol{\lambda}$ can be found.

To make this more concrete, we briefly look at the relatively simple case of the B_z field produced by two conducting ribbons, infinite along x [41], with surface current flowing in opposite directions along x. The surface current $K(z)$ is chosen to be even so that all odd derivatives of B_z will be zero when evaluated at $\mathbf{r_0}$, for $\mathbf{r_0}$ on the axis of symmetry. In addition, it can be shown that,

$$\left[\frac{\partial^2\Phi(\mathbf{r},z')}{\partial z^2}\right]_{\mathbf{r}=\mathbf{r_0}} \propto \left[\frac{\partial^2\Phi(\mathbf{r},z')}{\partial y^2}\right]_{\mathbf{r}=\mathbf{r_0}} \tag{11}$$

$$\left[\frac{\partial^4\Phi(\mathbf{r},z')}{\partial z^4}\right]_{\mathbf{r}=\mathbf{r_0}} \propto \left[\frac{\partial^4\Phi(\mathbf{r},z')}{\partial y^4}\right]_{\mathbf{r}=\mathbf{r_0}} \propto \left[\frac{\partial^4\Phi(\mathbf{r},z')}{\partial z^2\partial y^2}\right]_{\mathbf{r}=\mathbf{r_0}}. \tag{12}$$

Then, in order to homogenize B_z, we can impose the constraints:

$$\left[\frac{\partial^2 B_z(\mathbf{r})}{\partial z^2}\right]_{\mathbf{r}=\mathbf{r_0}} = \left[\frac{\partial^4 B_z(\mathbf{r})}{\partial z^4}\right]_{\mathbf{r}=\mathbf{r_0}} = 0. \tag{13}$$

Therefore only two coefficients in the expansion of K,

$$\lambda_1 = \frac{\begin{vmatrix} b_1 & c_{12} \\ b_2 & c_{22} \end{vmatrix}}{\begin{vmatrix} c_{11} & c_{12} \\ c_{21} & c_{22} \end{vmatrix}} \text{ and } \lambda_2 = \frac{\begin{vmatrix} c_{11} & b_1 \\ c_{21} & b_2 \end{vmatrix}}{\begin{vmatrix} c_{11} & c_{12} \\ c_{21} & c_{22} \end{vmatrix}} \tag{14}$$

with

$$b_N = \int_{-L/2}^{L/2} \left[\frac{\partial^{2N}\Phi(\mathbf{r},z')}{\partial z^{2N}}\right]_{\mathbf{r}=\mathbf{r_0}} dz', \tag{15}$$

$$c_{Nn} = -\int_{-L/2}^{L/2} f_n(z') \left[\frac{\partial^{2N}\Phi(\mathbf{r},z')}{\partial z^{2N}}\right]_{\mathbf{r}=\mathbf{r_0}} dz', \tag{16}$$

are enough to create a homogeneous field with sixth-order errors.

Following this procedure, a solution to the surface current is found and it only remains to be translated into wire spacing. While in theory any homogeneity can be found, physical limitations such as resolution of construction, will constrain the maximum achievable value. Note on choosing the number of terms in the surface current expansion: the larger the number of terms, or λ values, the better the homogeneity, but at a cost of more rapidly varying surface current with z; the smaller the number of terms, the more stable the solution and the easier it is to convert to a wire distribution with a small number of wires. In practice, we started with a two term expansion, then increased the number until the desired homogeneity could be reached.

Using the designed surface current, a field coil can be constructed from $\mathcal{N}$ wires, where $\mathcal{N}$ is chosen to be even for convenience. The current per wire is then:

$$I \equiv \frac{1}{\mathcal{N}} \int_{-L/2}^{L/2} K(z)dz. \tag{17}$$

Discretization is initially accomplished through an iterative approach, after which, wire positions are allowed to vary slightly to further optimize homogeneity. At first, the central two wires are set apart by:

$$dz_0 = \frac{I}{K(0)}, \tag{18}$$

then wires are placed around a central axis with positive positions given by:

$$z_1 = \frac{dz_0}{2} \quad \text{(first wire)}, \tag{19}$$

$$z_2 = z_1 + dz_1, \quad \text{where} \quad dz_1 = \frac{I}{K(z_1 + \frac{dz_0}{2})} \quad \text{(second wire)}, \tag{20}$$

$$z_3 = z_2 + dz_2, \quad \text{where} \quad dz_2 = \frac{I}{K(z_2 + \frac{dz_1}{2})} \quad \text{(third wire)}, \tag{21}$$

$$\vdots$$

$$z_{n+1} = z_n + dz_n, \quad \text{where} \quad dz_n = \frac{I}{K\left(z_n + \frac{dz_{n-1}}{2}\right)} \quad ([\mathrm{n}+1]^{\mathrm{th}} \text{ wire}). \tag{22}$$

The negative wire positions are $z_{-n} = -z_n$.

With a larger $\mathcal{N}$, the surface current can be better represented, but a smaller $\mathcal{N}$ is easier to construct. In practice, we started with a smaller $\mathcal{N}$, optimized the homogeneity numerically and rounded wire positions to the resolution of the construction technique, then increased the number of wires until the desired homogeneity could be reached.

3. Physical implementation

3.1. Rectangular field coil for magnetometer array tuning

The rectangular field coil was made to provide a homogeneous field over a half-meter-long array of Twinleaf magnetometers [8,42,40]. The magnetometers were in a crossed pump–probe configuration and used ^{87}Rb atoms. The open geometry, shown in Fig. 2, allowed for easy placement of the magnetometers, along with their accompanying optical fibers. The field is used to control the resonance frequency of the magnetometers in the array and its sensitivity is inversely proportional to linewidth of each sensor. Therefore, the target is to ensure that the field coil does not significantly increase the linewidth. The natural linewidth of each magnetometer, dominated by atomic and wall collisions is < 0.3 kHz. Considering a range of 0–5 MHz, which covers common explosives detectable by NQR [43], a homogeneity of at least 6×10^{-5} is desired. A set of six small flexible coils [42,40], wrapped around each magnetometer, compensate locally for zeroth order variation in B_x, B_y, B_z and first order variations in B_z. Therefore only second and higher order field variations were minimized. Alternately, one could consider creating 2nd and 4th order local correction coils, however this would increase the complexity of the system substantially, particularly for an array with many magnetometers. Each additional local coil requires its own power supply and increases the difficulty of shimming the array, done globally since the local field coils produce fields not only on the target magnetometer but on its neighbors as well.

The designed surface current density for the tuning coil was

$$K(z) = K_0\left[1 + \lambda_1 \cos\left(\pi\frac{z}{L}\right) + \lambda_2 \cos\left(3\pi\frac{z}{L}\right)\right] \tag{23}$$

with $L = 8.2$ cm, $\lambda_1 = -0.434, \lambda_2 = 0.049$, where K_0 was chosen to match the desired field strength along the central axis. The surface current was constrained to run over a rectangular surface $x = 78.7$ cm $\times$ $y = 2.9$ cm. The height was chosen to accommodate the magnetometer's height and the width to accommodate the length of the array. The length $L = 8.2$ cm was chosen for convenience in construction and to properly house the magnetometer array.

Fig. 3 below compares the designed surface current to the effective surface current from the wires, $\frac{I_0}{dz_n}$ centered between the n^{th} and the $(n+1)^{th}$ wire. Also shown is the predicted B_z homogeneity for two positions of the magnetometers, at 4 and 25 cm. Since the field is symmetric along y, the field homogeneity at only the top surface and middle of the magnetometer is shown. The homogeneity is constrained within $\pm 3 \times 10^{-5}$ for both magnetometer positions, neglecting first order variations. For comparison, using the same number of wires spread evenly over the same L causes the homogeneity to be degraded by two orders of magnitude.

3.1.1. Construction

The rectangular coil was constructed with two long narrow slats of FR4, a type of composite epoxy laminate, corresponding to the dimensions given above. Because the magnetometer array operated unshielded, x and y Earth's field compensation coils were also grooved into the slats. A Gerber Dimensions 200 CNC router [44], with a precision of 0.03 mm, was used to make the grooves for the 22-gauge wires. Two centimeter long spacers connected the slats and acted as guides for the magnetometers' placement.

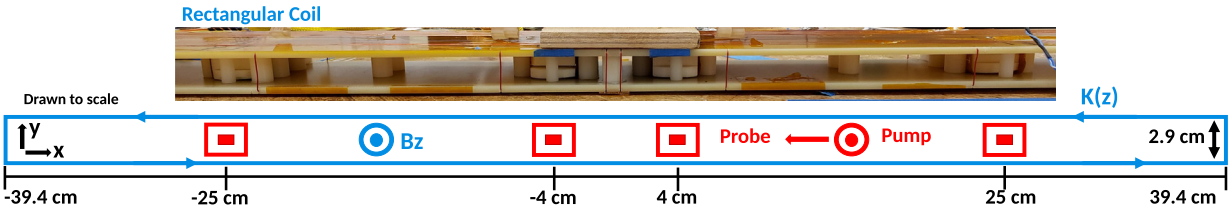

Fig. 2. Four magnetometers sit inside tuning and Earth's field compensation coils in the above photo. In the schematic, the active volume of each magnetometer is shown as a filled-in red square and the cross-section of the designed rectangular tuning coil is shown in blue with the direction of current flow. In this configuration, a magnetometer can detect B_x and B_y fields oscillating at its tuning frequency. (For interpretation of the references to colour in this figure legend, the reader is referred to the web version of this article.)

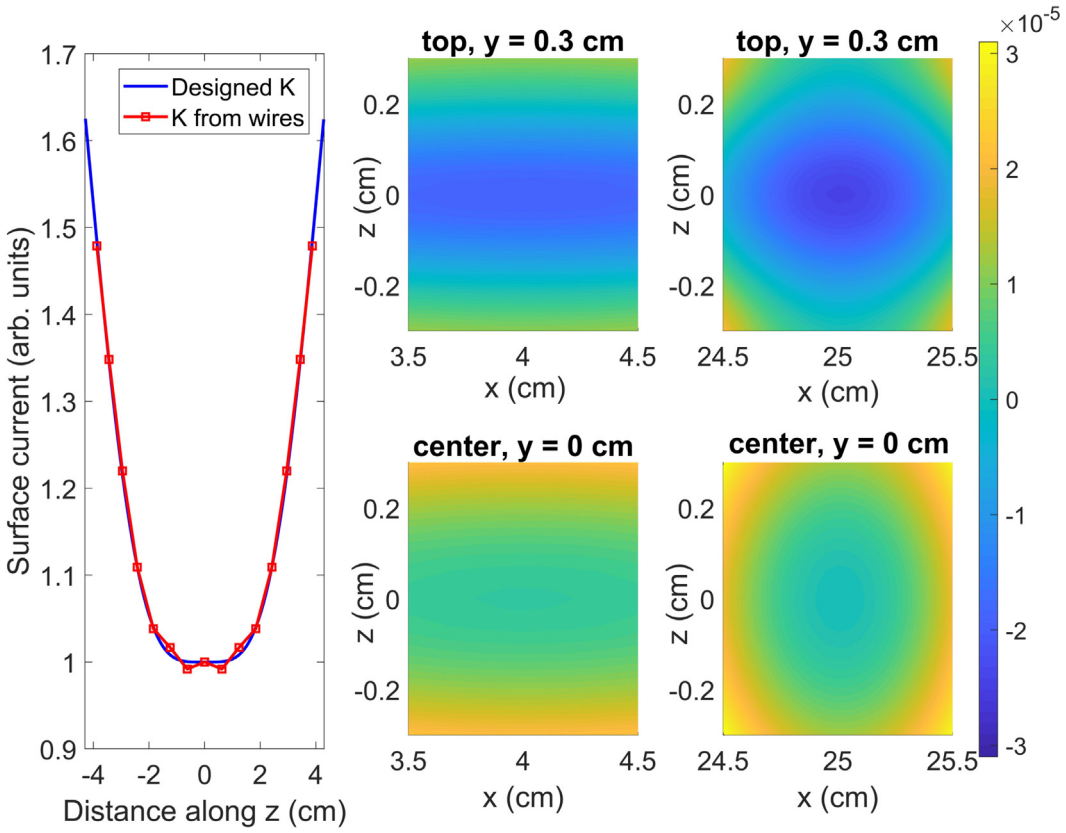

Fig. 3. A surface current K, shown to the left as a solid blue line, is designed to flow around a half-meter long array of magnetometers; details given in the text. It is converted to a 16-turn wire, resulting in an effective K shown as open red dots. To the right is the field homogeneity for the magnetometers, $1.0 \times 0.6 \times 0.6$ cm^3 active region, calculated for discrete wire positions. Values are shown for $x = 4$ cm, middle graphs, and $x = 25$ cm, far right graphs. With small local field coils, the B_z field can easily be adjusted to zeroth and first order in position. Therefore the linear term has been removed from the calculation and normalization is with respect to the local magnetic field. (For interpretation of the references to colour in this figure legend, the reader is referred to the web version of this article.)

3.2. Solenoid

A long solenoid was designed to shield an external sensor while maintaining a strong and uniform RF excitation field inside as shown in Fig. 1b. The target sensor to be used is a double-cell atomic gradiometer with crossed pump and probe beams [45] as shown in Fig. 1c; the linear magnetometer array, described in the section above, is used only in testing the operation of the solenoid. The static tuning field and the pump beam would be applied along the solenoid axis, so that sensor is only sensitive to the radial component. The dimensions of the homogeneous outside region were chosen based on the active volume of each magnetometer with 1 cm of separation between them. Each cell is $2.5 \times 1.5 \times 1$ cm^3, with the longest dimension placed along the solenoid axis and the next longest outwards from the solenoid. Furthermore, in order to accommodate the oven of the gradiometer, the minimized volume was made to be 1 cm away from the edge of the coil. Constraints up to fourth-order field variations in space were imposed and the designed surface current was found to be:

$$K(z) = K_0\Big[1 + \lambda_1 \cos\left(\pi\frac{z}{L}\right) + \lambda_2 \cos\left(3\pi\frac{z}{L}\right) + \lambda_3 \cos\left(5\pi\frac{z}{L}\right) + \lambda_4 \cos\left(7\pi\frac{z}{L}\right)\Big] \quad (24)$$

with $\lambda_1 = -0.647$, $\lambda_2 = 0.158$, $\lambda_3 = -0.045$, $\lambda_4 = 0.007$. The coil length $L = 42.0$ cm, a radius of $a = 1.41$ cm, and K_0 were chosen to match the parameters of a uniform solenoid with 4 turns/cm.

As shown in Fig. 4, the effective surface current after discretization compares well to the designed surface current. Also shown is

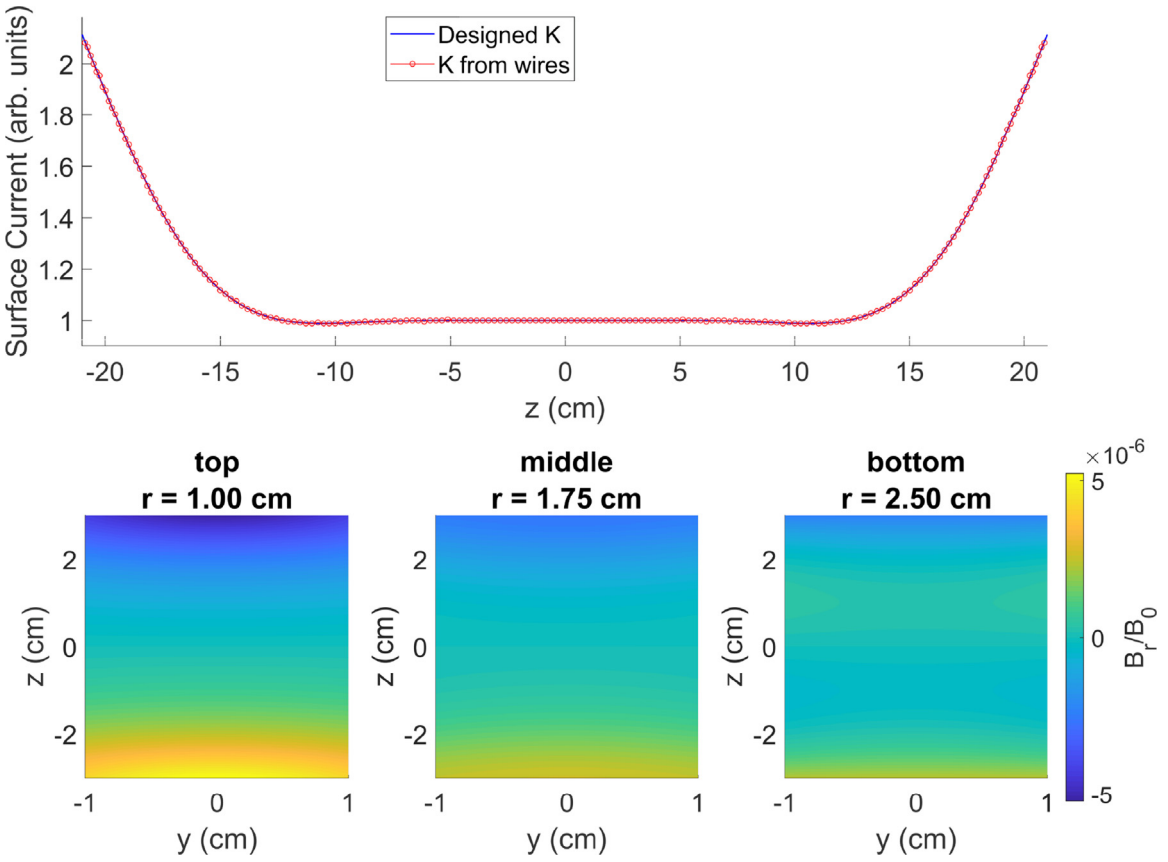

Fig. 4. A surface current K, shown as a solid blue line in the upper graph, is designed to span the surface of a 42 cm cylinder. It is converted to a 190-turn coil, resulting in an effective K shown as open red dots, that matches well with the designed K. In the lower graphs, the radial field calculated from discrete wire positions, is normalized with respect to the internal axial field B_0. Calculated values are shown for displacements $x = 1$ cm (top), 1.75 cm (middle), and 2.5 cm (bottom) from the edge of the coil. (For interpretation of the references to colour in this figure legend, the reader is referred to the web version of this article.)

the predicted B_r homogeneity at various positions in the target region, with "top" being closest to the coil. For comparison, the radial field outside a solenoid with uniform windings can be estimated by $\frac{2z}{L}\left(\frac{a}{L}\right)^2$, when normalized to the internal field and z is the displacement from the axis center [46]. Using this model, the optimized solenoid improves the homogeneity by two orders of magnitude (from $\pm 2 \times 10^{-4}$ to $\pm 5 \times 10^{-6}$) compared to a standard solenoid with uniform winding, assuming the same radius and length and $z = \pm 3$ cm.

3.2.1. Construction

The model for a coil guide with a non-homogeneous wire density was designed using CAD software and printed using a Form 2 stereolithographic (SLA) 3D printer with temperature-resistant resin [47]. Due to the printer size the solenoid was divided into three pieces with integrated flanges. The pieces were joined as shown in Fig. 5.

It was found that the wire-guide grooves could only be correctly printed if the solenoid was in a horizontal position with respect to the printing platform. If not, the grooves would either collapse upon themselves or need supports inside, which would contort the wire positions. To make the printing orientation possible a long beam was added to the design of each piece along the length and the majority of supports were placed on this beam. Tunnels through the beam were created around the grooves to allow for 28-gauge wire wrapping. The minimum controlled increment of the Form 2 in the horizontal plane [47] was taken as 10 μm and used for the calculations shown in Fig. 4.

4. Experimental method

4.1. Rectangular field coil for magnetometer array tuning

To test the homogeneity of the large area, static field coil, the linewidth of the magnetometers was measured at two different locations within the coil structure for a distribution of frequencies from 300 kHz to 4 MHz. As shown in Fig. 2, the two positions measured were 4 cm and 25 cm from the center of the coil. This was performed with the vapor cells at a low temperature so that the relaxation rate of the polarized atoms would be dictated by field inhomogeneities. At low temperatures the relaxation rate is lower due to a decreased atomic number density (and therefore atomic collisions).

4.2. Solenoid

Because the 3D printed solenoid is meant to be used as an RF excitation coil for frequencies close to a MHz, it was tested with AC currents at 1 MHz. However, a comparison between the DC and AC field was necessary to evaluate the extent to which the coil's reactance caused the observed field to differ from its design target.

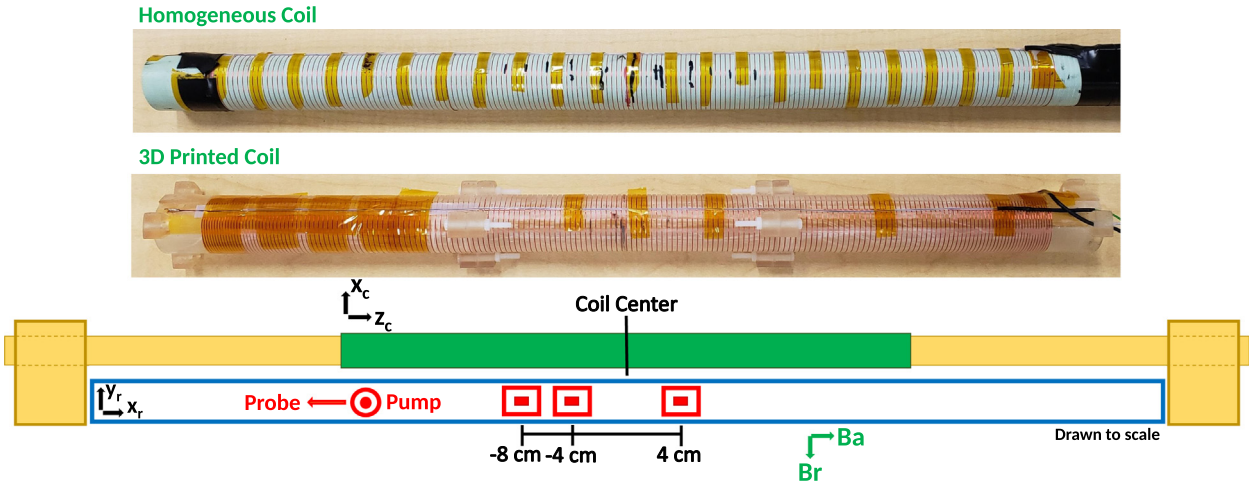

Fig. 5. Photos of the two different types of solenoid studied are at the top, and represented in green in the field testing schematic below. On top of the array of RF magnetometers seen in Fig. 2, the solenoid under test is held by a tube over which it can slide. Because of the tuning field's direction, the axial and radial components (B_a, B_r) of the external magnetic field can be measured simultaneously.The coordinate system subscripted with *c* refers to the coordinate system used for the design of the 3D printed coil, whereas the coordinate system subscripted with *r* refers to that of the r.ectangular coil.

4.2.1. DC measurements

In order to measure the direct current field produced by the printed coil, a Hall probe was used inside of it and a fluxgate magnetometer was used for both axial and radial components of the external field. Power was supplied by a Bipolar Operational Amplifier (BOP) and a 0.1 Ω resistor was connected in series to monitor the current.

The fluxgate magnetometer was held static while the coil was translated over it in a direction along the coil length. At each position, the current was varied between ±4 A to find the field values per current. Both a coil with homogeneous current density and the printed coil were tested and compared. Background Earth's field measurements were made before and after each data point, in order to quantify error due to field drift.

4.2.2. AC measurements

To measure the magnetic field produced by the printed coil with an AC current, the solenoid was translated along a fixed tube over the array of stationary RF atomic magnetometers with the pumping direction perpendicular to length. As shown in Fig. 5, 3 out of 4 magnetometers of the target array were used. The middle one was positioned 8 cm away from one at its side and 4 cm away from the other. By placing the coil center between pairs of sensors, symmetric positions such as ±2 cm could be measured and all 3 magnetometers could be used simultaneously. Due to the perpendicularity between axial and radial components of field outside, both were detected in each measurement taken. Once measurements with both pairs were done the coil was flipped about its center and these were repeated. Reference datasets were also performed before and after the solenoid datasets in order to calibrate each sensor and ensure its resonance frequency had not shifted from the test frequency. The inner field was measured through Faraday's induction with a small sniffer coil. The same approach was taken to measure the field from the comparison coil with homogeneous current density.

Furthermore, in order to confirm that any disagreement between AC and DC configurations was not caused by reactive effects, an AC experiment similar in position increments to the DC configuration was performed. The coil was displaced along its length on top of a single magnetometer for this experiment.

5. Results

5.1. Rectangular field coil for magnetometer array tuning

As shown in Fig. 6, by measuring the linewidth as a function of field strength, the homogeneity in B_z was measured to be on the order of 10^{-5}. The magnetometers' resonance frequency is $f = \frac{\gamma_{Rb}}{2\pi} B_z$ and the field contribution to the linewidth is $\Delta f = \gamma_{Rb} \Delta B_z$ where $\frac{\gamma_{Rb}}{2\pi} = 7$ GHz/T. Therefore, the homogeneity over the magnetometers due to the coil is the slope of linewidth vs resonant frequency. In Fig. 6, the error bar in the linewidth is much smaller than the scatter around the line. The error bar in the linewidth is due to the fit of the data. Fitting examples are shown in the bottom graphs of Fig. 6 and details for the fits are given below. The scatter, on the other hand, reflects the difficulty of consistently shimming the magnetometer with the local linear-gradient correction coils. A magnetometer placed further out from the center requires more correction, therefore it is unsurprising that the scatter is greater for this position. The error bars in the slope, and therefore in the reported homogeneity, take into account the scatter of the data. While these error bars are large, it is nevertheless clear that the homogeneity is on the order of 10^{-5}.

Furthermore, as the field increases the Zeeman resonances, corresponding to transitions between adjacent hyperfine sublevels *m*, go from being unresolved to partly resolved to fully resolved [8]. At higher fields, the difference in Zeeman resonance frequencies is much larger than the linewidth of an individual peak, it is easy to fit the central part of the dominant peak to a Lorentzian and to find the full-width-half-max (FWHM) width. The spectra taken with frequencies greater than or equal to 2 MHz correspond to this condition; see Fig. 6(d). When the splitting between *m* sublevels is much smaller than the linewidth, as is the case for $f \leqslant 0.5$ MHz, there is only a single symmetric peak corresponding to all the $F = 2$ hyperfine levels; see Fig. 6 (b). Only the central part of this peak is fit to a Lorentzian to avoid any possible contribution from the $F = 1$ transitions, which are clearly distinct at $f = 0.3$ MHz. For the case where the splitting is comparable to the linewidth, for instance as in Fig. 6(c), the observed peak is not symmetric. This asymmetric peak is fit to two peaks, and the linewidth of the dominant peak is taken as the linewidth; this methodology is only rea-

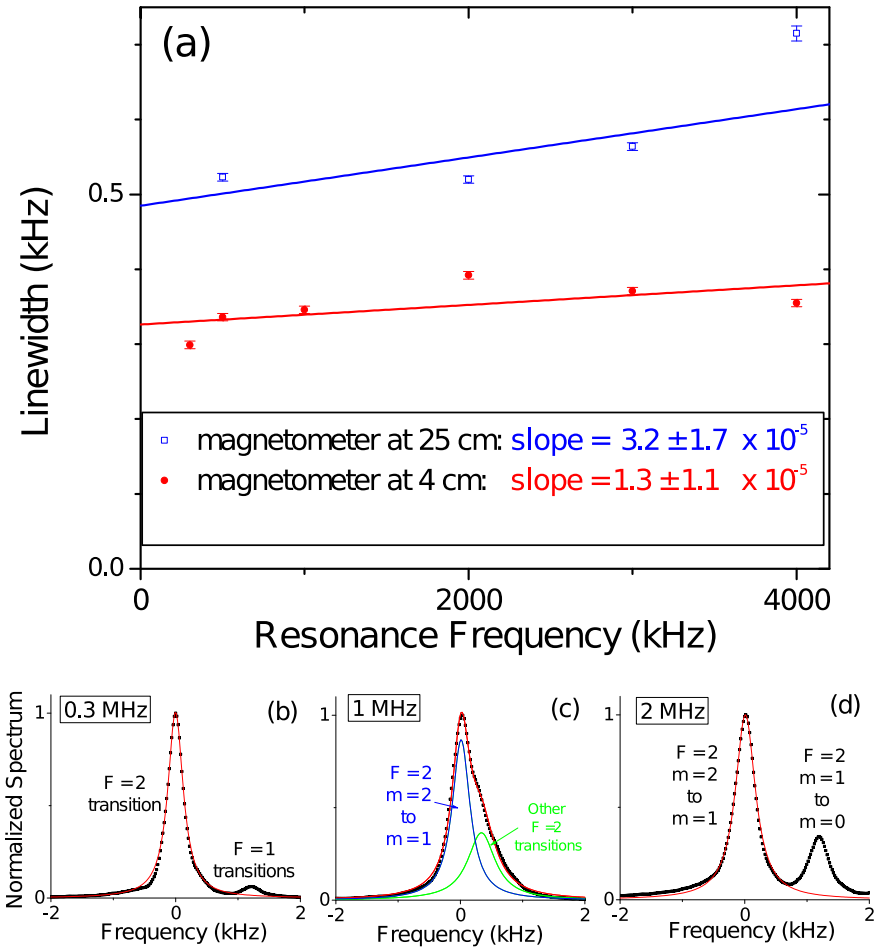

Fig. 6. Graph (a) displays the linewidth versus resonance frequency for both a magnetometer close to the center of the coil and one close to edge. The slope gives the homogeneity of the field and is consistent with 10^{-5} level predicted by theory for both positions. Graphs (b)-(d) shows different ways of fitting the data, depending on the resolution of the Zeeman transitions. Spectra are obtained with tip angles of 0.3 rad.

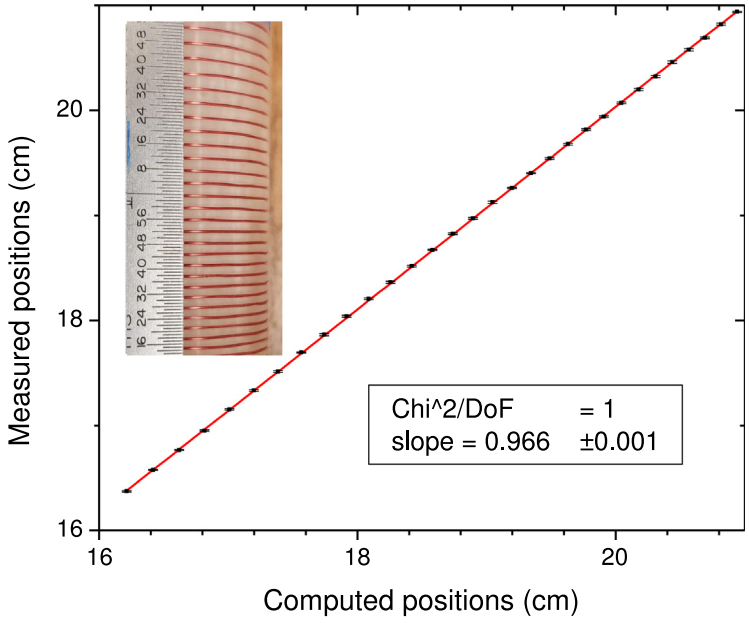

Fig. 7. By using a high-resolution camera (image shown in inset), and image processing software, the wire positions were measured and compared to theory. The distribution in the points was used to find an error bar of 80 μm; this puts an upper bound on the accuracy of the printer.

sonable in the case of high polarization when one peak clearly dominates.

5.2. Solenoid

As shown in Fig. 7, the printed wire positions, obtained from image processing software on an image with resolution of 27 μm/pixel, compare well to the computed positions. The slope is less than unity due to an overall 1% length shrinkage of the coil upon curing and the thickness of the ruler. The latter causes the coil to be displaced behind the ruler and the distance between wires to appear smaller.

The field measurements, taken with the atomic magnetometers described in Section 3.1, are shown below in Fig. 8. The linear gradient present for the radial field of the printed coil is due to imperfections in the coil. Two imperfections were clearly visible due to printing the coil in three separate pieces: 1) A non-flat contact between flanges led to a small, 0.3°, angular displacement between pieces 2) the support beam contracted more than the solenoid leading to warping of the wire grooves near the flanges. Calculations show both effects would contribute a non-zero radial component, but were not comparable in magnitude to the observed field. In addition when the field coil was rotated about its axis and sensors left in place, the observed radial field did not change significantly. Both imperfections would have yielded asymmetric results, but observed azimuthal symmetry in the field suggested that the radius might not be uniform. When measured, it was found that the radius at the center of each piece was slightly smaller than the edges by about 0.1 mm.

Furthermore, Fig. 9 shows how the radial field measurements for both DC and AC configurations of the homogeneous coil agree with each other and theoretical calculations. The printed coil measurements show a radial component of field that is much larger than its expected value, ~10^{-6} of the internal axial field. However, there is agreement between AC and DC measurements indicating that the discrepancy is not due to reactive effects.

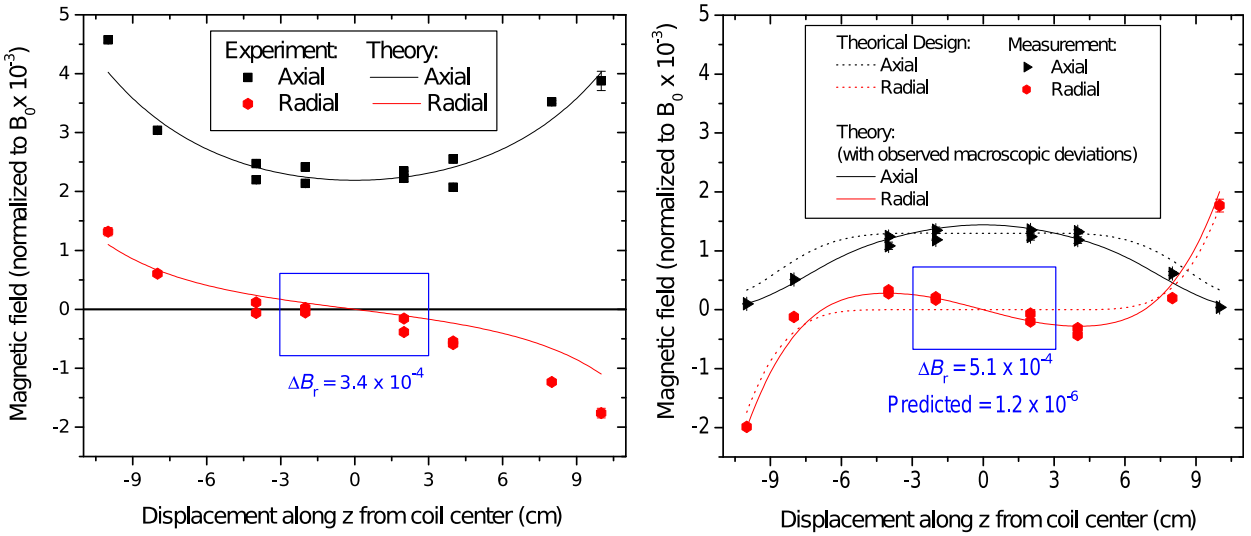

Fig. 8. Simultaneous measurements of both radial (red) and axial (black) fields are shown for the uniform coil, on the left, and printed coil on the right. Experiment is in reasonable agreement with predictions (solid line) when radial perturbations of the 3D printed coil are taken into account. The perturbations led to significant deviation from the design target (dotted line). All measurements were taken 2.5 cm from the coil edge.

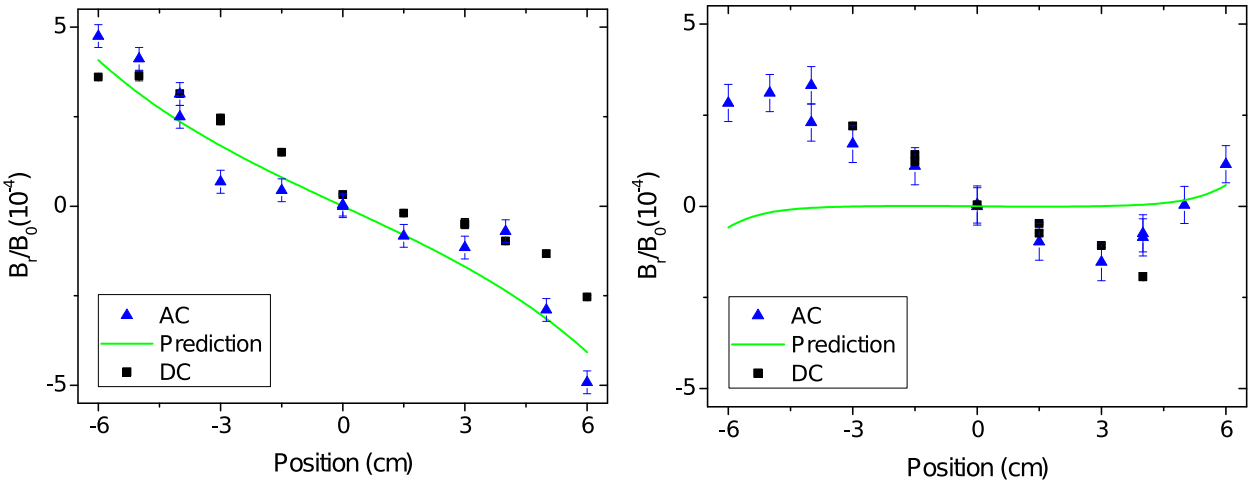

Fig. 9. Measurements of the DC field (black) agree with AC values (blue). Field measurements for the uniform coil (left) agree with theory (green), as is expected. In contrast, for the printed coil (right), the fields are different from design expectations, as is explained in more detail in the text. All measurements were taken 2.5 cm from the edge of the coil.

6. Conclusion

In conclusion, we have demonstrated how the proposed double expansion method can be implemented in the design of two coils with only fifth order errors in homogeneity or better. For the long solenoid, the radial field measured in the outside leakage-free volume was found to be 5.1×10^{-4} of the internal axial field, two orders of magnitude larger than expected. Possible variation in wire positions, up to 80 μm from 3D printer resolution, could not account for this discrepancy.

All three pieces of the solenoid were scanned for other defects of construction, and while some were found, a distortion of the radius in each piece was the primary contribution to the field difference. The 1% hourglass distortion is in accordance with warping in the curing process. Such warping has been observed by other researchers [48]. After all defects in the coil were modeled into theoretical predictions, these matched experimental values closely. Therefore, we conclude that in this case a fault of construction, not of methodology, occurred. The results show that while 3D printing technology can be used to manufacture difficult geometries at a larger scale, its precision is still limited by uncertainty in the curing process.

In contrast, the field from a CNC milled rectangular coil was found to closely match the designed values. With local zero and first-order correction coils, the homogeneity was found to be $3.2 \pm 1.7 \times 10^{-5}$ over 50 cm, which meets all design requirements. Therefore, we conclude that coefficients of a designed surface current expansion can be successfully made to cancel out higher order terms in an expansion of the target magnetic field. The achievable homogeneity is only limited by physical restrictions of construction and, as shown by two experimental examples above, the method proves to be specially suited for cases were unconventional geometries are needed.

Declaration of Competing Interest

The authors declare that they have no known competing financial interests or personal relationships that could have appeared to influence the work reported in this paper.

Acknowledgements

This work was supported by the National Science Foundation (award #1711118) as well as the US Army: Night Vision and Electronic Sensors Directorate (MTEQ: #W909MY-12-D0008/0024).

References

[1] G.P. Wong, C.H. Tseng, V.R. Pomeroy, R.W. Mair, D.P. Hinton, D. Hoffmann, R.E. Stoner, F.W. Hersman, D.G. Cory, R.L. Walsworth, A system for low field imaging of laser-polarized noble gas, J. Magn. Reson. 141 (1999) 217–227.
[2] E. Durand, G. Guillot, L. Darrasse, G. Tastevin, P.J. Nacher, A. Vignaud, D. Vattolo, J. Bittoun, CPMG measurements and ultrafast imaging in human lungs with hyperpolarized helium-3 at low field (0.1 T), Magn. Reson. Med. 47 (2002) 75–81.
[3] L.L. Tsai, R.W. Mair, M.S. Rosen, S. Patz, R.L. Walsworth, An open-access, very-low-field MRI system for posture-dependent 3He human lung imaging, J. Magn. Reson. 193 (2008) 274–285.
[4] G. Bison, N. Castagna, A. Hofer, P. Knowles, J.-L. Schenker, M. Kasprzak, H. Saudan, A. Weis, A room temperature 19-channel magnetic field mapping device for cardiac signals, Appl. Phys. Lett. 95 (2009) 173701, https://doi.org/10.1063/1.3255041.
[5] R. Wyllie, M. Kauer, G.S. Smetana, R.T. Wakai, T.G. Walker, Magnetocardiography with a modular spin-exchange relaxation-free atomic magnetometer array, Phys. Med. Biol. 57 (2012) 2619.
[6] Cort N. Johnson, P.D.D. Schwindt, M. Weisend, Multi-sensor magnetoencephalography with atomic magnetometers, Phys. Med. Biol. 58 (2013) 6065–6077.
[7] O. Alem, R. Mhaskar, R. Jiménez-Martínez, D. Sheng, J. LeBlanc, L. Trahms, T. Sander, J. Kitching, S. Knappe, Magnetic field imaging with microfabricated optically-pumped magnetometers, Opt. Express 25 (2017) 7849–7858.
[8] Robert J. Cooper, David W. Prescott, Garrett J. Lee, Karen L. Sauer, RF atomic magnetometer array with over 40 db interference suppression using electron spin resonance, J. Magn. Reson. 296 (2018) 36–46.
[9] Cameron Deans, Luca Marmugi, Ferruccio Renzoni, Active underwater detection with an array of atomic magnetometers, Appl. Opt. 57 (2018) 2346–2351.
[10] Niall Holmes, Tim M. Tierney, James Leggett, Elena Boto, Stephanie Mellor, Gillian Roberts, Ryan M. Hill, Vishal Shah, Gareth R. Barnes, Matthew J. Brookes, Richard Bowtell, Balanced, bi-planar magnetic field and field gradient coils for field compensation in wearable magnetoencephalography, Sci. Rep. 9 (2019) 14196.
[11] V. Bangert, P. Mansfield, Magnetic field gradient coils for NMR imaging, J. Phys. E: Sci. Instrum. 15 (1982) 235–239.
[12] B.H. Suits, D.E. Wilken, Improving magnetic field gradient coils for NMR imaging, J. Phys. E: Sci. Instrum. 22 (1989) 565.
[13] Robert Turner, Gradient coil design: A review of methods, Magn. Reson. Imaging 11 (1993) 903–920.
[14] Michael Poole, Pierre Weiss, Hector Sanchez Lopez, Michael Ng, Stuart Crozier, Minimax current density coil design, J. Phys. D: Appl. Phys. 43 (2010) 095001.
[15] Milan Wayne Garrett, Axially symmetric systems for generating and measuring magnetic fields. part I, J. Appl. Phys. 22 (1951) 1091–1107, https://doi.org/10.1063/1.1700115.
[16] L.W. McKeehan, Combinations of circular currents for producing uniform magnetic fields, Rev. Sci. Instrum. 7 (1936) 150–153, https://doi.org/10.1063/1.1752099.
[17] J.R. Barker, New coil systems for the production of uniform magnetic fields, J. Sci. Instrum. 26 (1949) 273–275.
[18] Milan Wayne Garrett, Sergio Pissanetzky, Polygonal coil systems for magnetic fields with homogeneity of the fourth to the eighth order, Rev. Sci. Instrum. 42 (1971) 840–857, https://doi.org/10.1063/1.1685243.
[19] Joseph L. Kirschvink, Uniform magnetic fields and double-wrapped coil systems: Improved techniques for the design of bioelectromagnetic experiments, Bioelectromagnetics 13 (1992) 401–411, https://onlinelibrary.wiley.com/doi/pdf/10.1002/bem.2250130507.
[20] P. Kedzia, T. Czechowski, M. Baranowski, J. Jurga, E. Szcześniak, Analysis of uniformity of magnetic field generated by the two-pair coil system, Appl. Magnetic Resonance 44 (2013) 605–618.
[21] Wu. Wenfeng, Binquan Zhou, Gang Liu, Linlin Chen, Jing Wang, Jiancheng Fang, Novel nested saddle coils used in miniature atomic sensors, AIP Adv. 8 (2018) 075126, https://doi.org/10.1063/1.5036605.
[22] W. Wu, B. Zhou, Z. Liu, J. Wang, H. Pang, L. Chen, W. Quan, G. Liu, Design of highly uniform magnetic field coils based on a particle swarm optimization algorithm, IEEE Access 7 (2019) 125310–125322.
[23] R. Turner, A target field approach to optimal coil design, J. Phys. D: Appl. Phys. 19 (1986) L147–L151.
[24] R. Turner, Minimum inductance coils, J. Phys. E: Sci. Instrum. 21 (1988) 948–952.
[25] Michael A. Brideson, Larry K. Forbes, Stuart Crozier, Determining complicated winding patterns for shim coils using stream functions and the target-field method, Conc. Magnet. Resonance 14 (2002) 9–18, https://onlinelibrary.wiley.com/doi/pdf/10.1002/cmr.10000.
[26] M. Engelsberg, R.E. De Souza, C.M. Dias Pazos, The limitations of a target field approach to coil design, J. Phys. D: Appl. Phys. 21 (1988) 1062–1066.
[27] M. Engelsberg, Target-field approach for the design of power-efficient solenoidal magnets, Meas. Sci. Technol. 3 (1992) 1063–1067.
[28] Stuart Crozier, Stephen Dodd, Kurt Luescher, James Field, David M. Doddrell, The design of biplanar, shielded, minimum energy, or minimum power pulsed B0 coils, Magn. Reson. Mater. Phys., Biol. Med. 3 (1995) 49–55.
[29] Lawrence K. Forbes, Stuart Crozier, A novel target-field method for finite-length magnetic resonance shim coils: I. Zonal shims, J. Phys. D: Appl. Phys. 34 (2001) 3447–3455.
[30] J. Wang, B. Zhou, W. Wu, L. Chen, J. Fang, Uniform field coil design based on the target-field method in miniature atomic sensors, IEEE Sens. J. 19 (2019) 2895–2901.
[31] L. Cesnak, D. Kabat, A cylindrical coil with graduated current density for very homogeneous magnetic fields, J. Phys. E: Sci. Instrum. 5 (1972) 944–946.
[32] D. Kabat, L. Cesnak, J. Kokavec, Optimisation of inner-notch-corrected highly homogeneous superconducting solenoids and their comparison with other coil configurations, J. Phys. E: Sci. Instrum. 12 (1979) 652–657.
[33] S. Kruber, G.D. Farrher, E. Anoardo, Air core notch-coil magnet with variable geometry for fast-field-cycling NMR, J. Magn. Reson. 259 (2015) 216–224.
[34] R.J. Cooper, B.L. Mark, D.W. Prescott, K.L. Sauer, Improving the design of atomic magnetometer arrays for RF interference mitigation in NQR detection of explosives, Proc. SPIE 10182 (2017) 1018208.
[35] Russell A. Compton, Gradient-coil apparatus for a magnetic resonance system, (1984), uS Patent 4,456,881.
[36] K.H. Schweikert, R. Krieg, F. Noack, A high-field air-cored magnet coil design for fast-field-cycling NMR, J. Magn. Reson. 1969 (78) (1988) 77–96.
[37] Eric C. Wong, A. Jesmanowicz, James S. Hyde, Coil optimization for MRI by conjugate gradient descent, Magn. Reson. Med. 21 (1991) 39–48, https://onlinelibrary.wiley.com/doi/pdf/10.1002/mrm.1910210107.
[38] O. Lips, A.F. Privalov, S.V. Dvinskikh, F. Fujara, Magnet design with high B0 homogeneity for fast-field-cycling NMR applications, J. Magn. Reson. 149 (2001) 22–28.

[39] V.V. Yashchuk, J. Granwehr, D.F. Kimball, S.M. Rochester, A.H. Trabesinger, J.T. Urban, D. Budker, A. Pines, Hyperpolarized xenon nuclear spins detected by optical atomic magnetometry, Phys. Rev. Lett. 93 (2004) 160801.
[40] R.J. Cooper, D.W. Prescott, P. Matz, K.L. Sauer, N. Dural, M.V. Romalis, E.L. Foley, T.W. Kornack, M. Monti, J. Okamitsu, Atomic magnetometer multisensor array for RF interference mitigation and unshielded detection of nuclear quadrupole resonance, Phys. Rev. Applied 6 (2016) 064014.
[41] N. Gauthier, Magnetic field of an infinite current-carrying ribbon, Am. J. Phys. 56 (1988) 819–821, https://doi.org/10.1119/1.15456.
[42] Twinleaf LLC, http://www.twinleaf.com/ (2017).
[43] J.B. Miller, G.A. Barrall, Explosives detection with nuclear quadrupole resonance: An emerging technology will help to uncover land mines and terrorist bombs, Am. Sci. 93 (2005) 50–57.
[44] Gerber, www.gerbertechnology.com (2019).
[45] D.A. Keder, D.W. Prescott, A.W. Conovaloff, K.L. Sauer, An unshielded radio-frequency atomic magnetometer with sub-femtotesla sensitivity, AIP Adv. 4 (2014) 127159, https://doi.org/10.1063/1.4905449.
[46] Jason Farley, Richard H. Price, Field just outside a long solenoid, Am. J. Phys. 69 (2001) 751–754.
[47] Formlabs, www.formlabs.com (2020).
[48] D. Karalekas, A. Aggelopoulos, Study of shrinkage strains in a stereolithography cured acrylic photopolymer resin, J. Mater. Process. Technol. 136 (2003) 146–150.